

Ab initio study of phase stability, elastic anisotropy, and minimum thermal conductivity of MnB_2 in different crystal structures

Xiao-Fan Wang(王小凡), Yi-Xian Wang(王乙先), Zhuo Wang(王卓), Yu-Xuan Zhang(张宇轩), and Jian-Bing Gu(顾建兵)

Citation: Chin. Phys. B, 2024, 33 (**12**): 126103. DOI: 10.1088/1674-1056/ad925c
Journal homepage: http://cpb.iphy.ac.cn; http://iopscience.iop.org/cpb

What follows is a list of articles you may be interested in

Quasi-plastic deformation mechanisms and inverse Hall-Petch relationship in nanocrystalline boron carbide under compression

Zhen Yue(岳珍), Jun Li(李君), Lisheng Liu(刘立胜), and Hai Mei(梅海)
Chin. Phys. B, 2024, 33 (**8**): 086105. DOI: 10.1088/1674-1056/ad4989

Properties of radiation defects and threshold energy of displacement in zirconium hydride obtained by new deep-learning potential

Xi Wang(王玺), Meng Tang(唐孟), Ming-Xuan Jiang(蒋明璇), Yang-Chun Chen(陈阳春), Zhi-Xiao Liu(刘智骁), and Hui-Qiu Deng(邓辉球)
Chin. Phys. B, 2024, 33 (**7**): 076103. DOI: 10.1088/1674-1056/ad362b

Evolution of defects and deformation mechanisms in different tensile directions of solidified lamellar Ti-Al alloy

Yutao Liu(刘玉涛), Tinghong Gao(高廷红), Yue Gao(高越), Lianxin Li(李连欣), Min Tan(谭敏), Quan Xie(谢泉), Qian Chen(陈茜), Zean Tian(田泽安), Yongchao Liang(梁永超), and Bei Wang(王蓓)
Chin. Phys. B, 2022, 31 (**4**): 046105. DOI: 10.1088/1674-1056/ac1f0b

First-principles study of two new boron nitride structures: C12-BN and O16-BN

Hao Wang(王皓), Yaru Yin(殷亚茹), Xiong Yang(杨雄), Yanrui Guo(郭艳蕊), Ying Zhang(张颖), Huiyu Yan(严慧羽), Ying Wang(王莹), and Ping Huai(怀平)
Chin. Phys. B, 2022, 31 (**2**): 026102. DOI: 10.1088/1674-1056/ac0a69

Prediction of scandium tetraboride from first-principles calculations: Crystal structures, phase stability, mechanical properties,and hardness

Bin-Hua Chu(初斌华) and Yuan Zhao(赵元)
Chin. Phys. B, 2021, 30 (**7**): 076107. DOI: 10.1088/1674-1056/abe116

Ab initio study of phase stability, elastic anisotropy, and minimum thermal conductivity of MnB_2 in different crystal structures

Xiao-Fan Wang(王小凡)[1], Yi-Xian Wang(王乙先)[1,†], Zhuo Wang(王卓)[1], Yu-Xuan Zhang(张宇轩)[1], and Jian-Bing Gu(顾建兵)[2]

[1] *College of Science, Xi'an University of Science and Technology, Xi'an* 710054, *China*
[2] *School of Materials and Chemical Engineering, Zhongyuan University of Technology, Zhengzhou* 450007, *China*

(Received 26 June 2024; revised manuscript received 11 October 2024; accepted manuscript online 14 November 2024)

The phase stability, elastic anisotropy, and minimum thermal conductivity of MnB_2 in different crystal structures have been investigated by first-principles calculations based on density functional theory. The results found that $P6_3/mmc$ ($hP6$-MnB_2), $P6/mmm$ ($hP3$-MnB_2), $Pmmn$ ($oP6$-MnB_2), $R\bar{3}m$($hR3$-MnB_2), $Pnma$ ($oP12$-MnB_2), and $Immm$ ($oI18$-MnB_2) all exhibit mechanical and dynamic stability under environmental conditions, and the sequence of phase stability was $hP6 > hR3 > oP6 > oI18 > oP12 > hP3$. In addition, Vickers hardness calculations indicated that $hP6$, $hR3$, $oP6$, and $oI18$ of MnB_2 have potential as hard materials, while $hP3$ and $oP12$ are not suitable as hard materials. Moreover, the elastic anisotropy of different MnB_2 phases were also comprehensively investigated. It is found that the anisotropic order of bulk modulus is $oP12 > hP3 > hP6 > hR3 > oI18 > oP6$, while that of Young's modulus is $oP12 > hR3 > hP6 > oP6 > hP3 > oI18$. Furthermore, the minimum thermal conductivity of different MnB_2 phases was evaluated by means of Clarke's and Cahill's models. The results suggested that these MnB_2 diborides are all not suitable as thermal barrier coating materials.

Keywords: transition metal boride, mechanical properties, density functional theory

PACS: 61.50.Ah, 61.41.+e, 61.50.Ah **DOI:** 10.1088/1674-1056/ad925c

1. Introduction

Transition metal borides, as a new type of hard material, are expected to play an important role in developing abrasives, cutting tools, and wear-resistant coatings. Therefore, there has been considerable interest in transition metal boride materials in recent years, such as ReB_2,[1–3] MgB_2,[4,5] MnB_4,[6,7] and WB_2.[8,9] Among them, manganese borides have found widespread applications across various fields due to their numerous outstanding characteristics, including high strength, exceptional hardness, superconducting properties, heightened ferromagnetism, elevated melting point, thermodynamic stability, and resistance to corrosion by molten metals and glass.[10–13]

Normally, the valence electron-rich three-dimensional (3D) magnetic metal manganese combines with "electron-deficient" boron to create many boron-based solids with unique characteristics. These materials exhibit excellent multifunctional properties,[14] as well as magneto structural and electronic behaviors. So far, experiments have successfully synthesized various Mn–B compounds, such as MnB,[15,16] Mn_3B_4,[13,17] MnB_2,[11] MnB_3,[18] MnB_4,[7,19,20] and theoretically predicted MnB_{12}[21] featuring zigzag chains, honeycomb layers, and caged structures. Among them, MnB_2 has broad application prospects in industrial products due to its superior mechanical properties and has emerged as a research hotspot in recent years.[22–26]

As early as 1978, Cely *et al.*[22] evaluated the microhardness of the Mn–B system through experimental measurement methods and proposed the potential of MnB_2 as a hard material. Later, Asokamani *et al.*[23] investigated the electronic structure and bonding ground state properties of $hP3$-MnB_2 by using the self-consistent tight-binding linear muffin-tin orbital method. The results showed that the strong interaction between boron atoms p states is the main reason for the structural stability of $hP3$-MnB_2. And in 2009, Aydin *et al.*[24] revealed through theoretical studies that MnB_2 with the ReB_2-type structure ($hP6$-MnB_2) exhibits potential as a superhard material. Meanwhile, they found that the energy of $hP6$-MnB_2 was superior to the $hP3$-MnB_2, which indicated that $hP6$-MnB_2 should be the ground state at ambient conditions. Subsequently, Wang *et al.*[25] explored the physical properties and structural stability of Mn–B compounds using first-principles calculations. The results show that $hP6$-MnB_2 is the most stable structure at the ground state. Nevertheless, unfortunately, this phase has yet to be synthesized effectively for a long time, either through a high temperature and high-pressure approach or by the arc-melting approach.

Until 2012, Fan *et al.*[26] had studied the specific synthesized conditions of $hP6$-MnB_2 through first-principles lattice dynamics computations utilizing the quasi-harmonic approximation. It is found that accurate temperature control is the key to the synthesis of $hP6$-MnB_2, which can only be synthesized below 1020 K at normal pressure. Soon after, Gou *et al.*[11] investigated the stability of $hP3$-MnB_2 through exper-

†Corresponding author. E-mail: lsdwyx@163.com

© 2024 Chinese Physical Society and IOP Publishing Ltd

iments and first-principles calculations, and effectively synthesized a single crystal of *hP*3-MnB_2 via high-temperature and high-pressure experimental methods. Furthermore, Niu *et al.*[13] performed an extensive investigation on the Mn–B system from both theoretical and experimental aspects. The results further confirm the existence of the *hP*3-MnB_2 phase. Moreover, they pointed out that the experiment did not observe the formation of *hP*6-MnB_2 mainly because the sample was synthesized at high temperatures, while the *hP*6-MnB_2 becomes thermodynamically unstable above 747 °C. Recently, Xu *et al.*[12] studied the stable MnB_2 structure at 0 GPa–60 GPa through the structure prediction algorithm. They found that *hP*6-MnB_2 possesses the lowest enthalpy of formation at the ground state and transforms into *oI*18-MnB_2 at around 36.8 GPa.

As mentioned above, different phases have been controversial regarding the ground state structure of MnB_2 at 0 GPa. In addition, previous studies mainly used some known diboride structures to study the structural stability of MnB_2 under environmental conditions, so the research results are not comprehensive. Therefore, further research on this problem is necessary. In this work, we used the particle swarm optimization (PSO) algorithm[27] to investigate the crystal structure of MnB_2 at ambient pressure. The PSO algorithm identifies the ground state and metastable structures using only the chemical composition at a given pressure. The results showed that *hP*6-MnB_2, *hP*3-MnB_2, *hR*3-MnB_2, *oP*12-MnB_2, *oI*18-MnB_2, and *oP*6-MnB_2 all possess relatively low enthalpy values at 0 GPa, implying that these phases have good thermodynamic stability and may be metastable structures under environmental conditions. Among them, *oP*12-MnB_2 (with a space group of *Pnma*) has been proposed for the first time and has not been reported before. In order to acquire a comprehensive understanding of MnB_2 in different structures under environmental conditions, we further revisit their internal physical properties through *ab initio* calculations based on the density functional theory.

2. Computational details

Crystal structure predictions were carried out with simulation cells containing up to 4 formula units by using the PSO algorithm as implemented in the CALYPSO code.[28] This method can predict stable or metastable crystal structures based on a given chemical composition under specific external conditions. The first generation of structures was randomly generated by CALYPSO under symmetry constraints. Each structure adjusted its evolution speed and direction based on past experience. Local structure optimization allowed the randomly generated structures to reach local minima or potentially approach the global free energy minimum. To increase search efficiency, a certain proportion (the best 60% from the previous generation) of low-energy structures evolved into the next generation. In addition, to maintain the diversity of crystal space groups, the remaining 40% of structures were still randomly generated. So far, this method has been successfully applied to various materials.[29–31]

Ab initio calculations[32,33] were conducted employing the Perdew–Burke–Ernzerhof (PBE)[34] form of the generalized approximation (GGA) for the exchange–correlation functional with CASTEP code. Ultrasoft pseudopotentials (USPPs) are used to describe the electron–ion interactions, treating $2s^2 2p^1$ and $3d^5 4s^2$ as valence electrons for B and Mn atoms, respectively. To achieve absolute convergences, the electronic wave functions are expressed in terms of a plane wave basis set, utilizing an energy cutoff of 700 eV. For the Brillouin zone samplings, the Monkhorst–Pack *k*-point meshes are $17 \times 17 \times 6$, $10 \times 17 \times 9$, $14 \times 14 \times 12$, $13 \times 8 \times 9$, $18 \times 10 \times 5$, and $8 \times 8 \times 8$ for *hP*6-MnB_2, *oP*12-MnB_2, *hP*3-MnB_2, *oP*6-MnB_2, *oI*18-MnB_2, and *hR*3-MnB_2 conventional cells, respectively. The geometry optimizations are performed until the difference in energy and force is less than 5×10^{-6} eV/atom and 0.01 eV/Å. In addition, the phonon dispersion curves were calculated by using the finite displacement method[35,36] within the CASTEP code. To ensure that the force calculations were fully convergent, the supercell of all MnB_2 structures defined by the cutoff radius of 5.0 Å, and $2 \times 2 \times 2$, $2 \times 2 \times 1$, $3 \times 3 \times 3$, $2 \times 2 \times 1$, $2 \times 2 \times 1$, and $2 \times 2 \times 2$ *k*-point meshes were chosen for *hP*6-MnB_2, *oP*12-MnB_2, *hP*3-MnB_2, *oP*6-MnB_2, *oI*18-MnB_2, and *hR*3-MnB_2 supercells, respectively.

3. Results and discussion

3.1. Crystal structures and phase stability

Based on the structure search results, *hP*6-MnB_2, *hP*3-MnB_2, *hR*3-MnB_2, *oP*6-MnB_2, *oP*12-MnB_2, and *oI*18-MnB_2

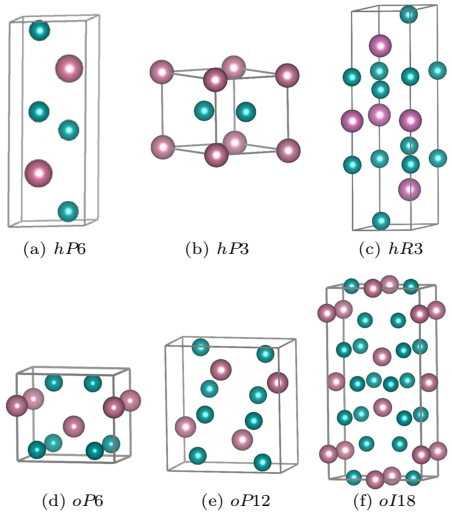


Fig. 1. Crystal structures of different MnB_2 phases. The purple and cyan spheres represent the Mn and B atoms, respectively.

all possess relatively low enthalpy values under environmental pressures. The crystal structures of them are depicted in Fig. 1. After full geometry optimization, the obtained equilibrium lattice parameters a, b, c, atomic coordinates, and cell volume V of various MnB_2 phases at 0 GPa are summarized in Table 1. Notably, our calculated a and c of $hP3$-MnB_2 are consistent well with other theoretical values,[13,25] and the errors with experimental data[11] are 2.13% and 1.25%, respectively. Meanwhile, the obtained atomic coordinates, and cell volume V of $hP6$-MnB_2 and $oI18$-MnB_2 are also consistent well with other available theoretical results.[12,24,25] This further validates the reliability of our calculated parameters.

Table 1. Calculated lattice parameters (in unit Å), atomic coordinates, cell volume V (in unit Å^3), and formation enthalpies ΔH (in unit eV) of different MnB_2 phases, together with the available experimental and theoretical data.

Space group	Symbol	Lattice parameters	Atom	x	y	z	V	ΔH	References
$P6_3/mmc$	$hP6$	$a=b=2.785$	B($4f$)	0.333	0.6667	0.55	23.43	–1.094	this work
		$c=6.976$	Mn($2c$)	0.333	0.667	0.75			
		$a=b=2.769$	B($4f$)	0.333	0.667	0.55			Cal.[24]
		$c=6.949$	Mn($2c$)	0.333	0.667	0.25			
		$a=b=2.778$	B($4f$)	0.333	0.667	0.55	23.25	–1.10	Cal.[25]
		$c=6.954$	Mn($2c$)	0.333	0.666	0.25			
$P6/mmm$	$hP3$	$a=b=2.944$	B($2d$)	0.333	0.666	0.5	22.57	–0.452	this work
		$c=2.998$	Mn($1a$)	0	0	0			
		$a=b=3.008$	B($2d$)	0.334	0.667	0.5			Exp.[11]
		$c=3.036$	Mn($1a$)						
		$a=2.987$	B($2d$)	0.333	0.667	0.5		–0.28	Cal.[13]
		$c=2.842$	Mn($1a$)	0	0	0			
		$a=b=3.054$					21.84	–0.45	Cal.[25]
		$c=2.702$							
$R\bar{3}m$	$hR3$	$a=b=c=3.864$	B($36i$)	0.299	0.299	0.299	23.57	–1.024	this work
			Mn($9d$)	0.500	0.499	0.499			
$Pmmn$	$oP6$	$a=2.791$	B($4e$)	0.500	0.701	0.866	23.57	–1.022	this work
		$b=4.386$	Mn($2a$)	0	0	0.633			
		$c=3.849$							
		$a=2.785$					23.39	–1.03	Cal.[25]
		$b=4.374$							
		$c=3.839$							
$Immm$	$oI18$	$a=2.782$	B($4h$)	0.5	0.180	0	134.57	–0.883	this work
		$b=4.656$	Mn($2d$)	1	0	0.131			
		$c=9.759$							
		$a=9.717$	B($4J$)	0.5	0.5	0.679			Cal.[12]
		$b=2.768$	Mn($2c$)	0.5	0.5				
		$c=4.940$							
$Pnma$	$oP12$	$a=5.237$	B2($4c$)	0.03	0.250	0.563	88.13	–0.622	this work
		$b=2.992$	B1($4c$)	0.268	0.750	0.394			
		$c=5.625$	Mn($4c$)	0.949	0.250	0.296			

In order to evaluate the relative stability of different MnB_2 structures, we initially computed their phonon dispersion curves using the finite displacement method. As depicted in Fig. 2, all MnB_2 phases have no imaginary phonon frequency appearing along the high symmetry lines, indicating that these structures are dynamically stable under ambient pressure. Meanwhile, we further calculated the formation enthalpy of different MnB_2 structures according to the formula $\Delta H = H(MnB_2) - H(Mn) - 2H(B)$,[29,30,37,38] where boron and manganese in α phase are used as reference structures. The obtained results are presented in Table 1, along with the other available theoretical data.[13,25] As shown, the obtained formation enthalpies of $hP6$-MnB_2, $hP3$-MnB_2, $hR3$-MnB_2, $oP6$-MnB_2, $oP12$-MnB_2, and $oI18$-MnB_2 are all negative, indicating that these structures possess thermodynamic stability and are potential metastable structures of MnB_2 under environmental conditions. Among them, $hP6$-MnB_2 has the lowest formation enthalpy of -1.094 eV/f.u, which is consistent with other theoretical results[13,25] and therefore should be the most energetically stable structure at 0 GPa. Meanwhile, the formation enthalpies of $hP3$-MnB_2, $hR3$-MnB_2, $oP6$-MnB_2, $oP12$-MnB_2, and $oI18$-MnB_2 are -0.452, -1.024, -1.022, -0.883, and -0.622 eV/f.u., respectively. Accordingly, the energetically stability order of MnB_2 is $hP6 > hR3 > oP6 > oI18 > oP12 > hP3$.

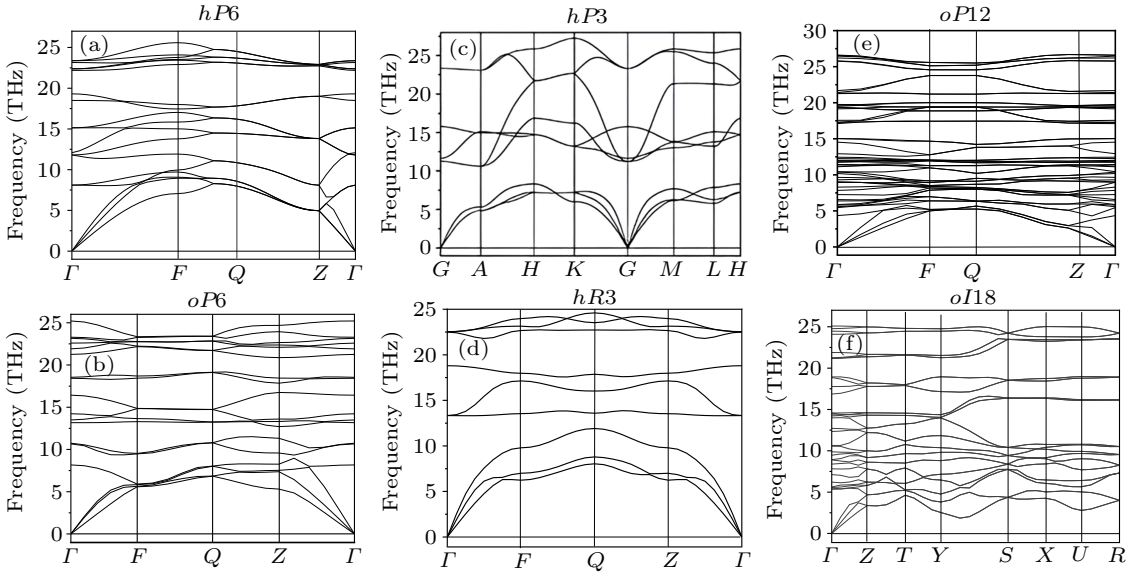


Fig. 2. Calculated phonon dispersion curves of different MnB_2 phases, where panel (c) was taken from Ref. [26].

3.2. Mechanical properties

3.2.1. Elastic constants and Vickers hardness

The elastic constants of different MnB_2 structures have been successfully determined using the stress–strain approach.[39] The calculated results are listed in Table 2, together with the other available theoretical results.[12,13,25] Obviously, the obtained elastic constants of *hP*6-MnB_2, *hP*3-MnB_2, and *oI*18-MnB_2 agree well with the existing theoretical values. Furthermore, the mechanical stability of different structures can be evaluated through Born–Huang's criteria.[40,41] In general, mechanical stability criteria for hexagonal structures *hP*6-MnB_2 and *hP*3-MnB_2 can be expressed as[41]

$$C_{44}>0,\quad C_{66}>0,\quad C_{11}-|C_{12}|>0,$$
$$(C_{11}+C_{12})C_{33}-2C_{13}^2>0. \tag{1}$$

While for trigonal crystal of *hR*3-MnB_2 is[42]

$$C_{11}-|C_{12}|>0,\quad (C_{11}+C_{22})C_{33}-2C_{13}^2,$$
$$(C_{11}-C_{12})C_{44}-2C_{14}^2>0. \tag{2}$$

And for orthorhombic phases of *oP*6-MnB_2, *oP*12-MnB_2, and *oI*18-MnB_2 are as follows:[43]

$$C_{11}>0,\quad C_{11}C_{22}-C_{12}^2>0,$$
$$C_{44}>0,\quad C_{55}>0,\quad C_{66}>0,$$
$$C_{11}C_{22}C_{33}+2C_{12}C_{13}C_{23}-C_{11}C_{23}^2-C_{23}C_{13}^2-C_{33}C_{12}^2>0. \tag{3}$$

It can be seen from Table 2 that the elastic constants of different MnB_2 structures all meet the corresponding mechanical stability criteria, suggesting that these phases should be mechanically stable.

Table 2. Calculated elastic constants C_{ij} (in unit GPa) of different MnB_2 phases, together with the available theoretical results.

Phase	C_{11}	C_{12}	C_{13}	C_{22}	C_{23}	C_{33}	C_{44}	C_{55}	C_{66}	References
*hP*6	492.0	166.7	100.1			862.5	273.2		163.6	this work
	495.2	167.0	96.4			867.3	276.4		164.1	Cal.[13]
	488.0	170.0	99.0			864.0	276.0		158.0	Cal.[25]
*hR*3	521.2	149.5	104.0			793.2	284.0		179.3	this work
*oP*6	482.2	186.1	98.8	490.9	101.6	794.0	253.6	180.8	194.0	this work
*hP*3	505.3	218.5	216.1			316.1	111.4		143.3	this work
	510	263	241			272	168		124	Cal.[25]
	615.4	168.4	111.7			393.6	122.1		223.5	Cal.[13]
*oI*18	645.6	189.1	174.9	425.1	190.5	642.5	269.3	186.0	163.2	this work
	653.0	178.0	170.0	442.0	189.0	643.0	273.0	161.0	166.0	Cal.[12]
*oP*12	283.6	106.8	167.6	566.4	245.1	541.4	204.0	99.93	119.2	this work

Moreover, the elastic constants C_{11}, C_{22}, and C_{33} usually represent the resistance to linear compression along the *a*, *b*, and *c* axes, respectively. As shown in Table 2, the calculated values of C_{33} for *hP*6, *hR*3, and *oP*6 are both larger than those of C_{11} and C_{22}, indicating that these phases are highly incompressible under uniaxial stress along the *c* axis and have stronger chemical bonds in the [001] direction. The opposite is true for *hP*3-MnB_2, it is very incompressible along

the a-axis and has stronger chemical bonds in the [100] direction because its C_{11} is much bigger than C_{33}. Moreover, the elastic constants of C_{44} and C_{66} represent the shear stress resistances along the [001] and [110] directions on the (100) plane, respectively. As illustrated in Table 2, the difference between C_{44} and C_{66} for different MnB_2 structures indicates the anisotropy of its shear modulus. Meanwhile, the higher the C_{44} value, the stronger the resistance to shear deformation. Accordingly, the shear deformation resistance order of MnB_2 is as follows: $hR3 > hP6 > oI18 > oP6 > oP12 > hP3$.

Similar to the recognized superhard material diamond, our calculated MnB_2 in $hP6$, $hR3$, and $oP6$ phases possess comparable C_{33} values, which means that these MnB_2 phases may also be potentially hard materials. Therefore, we further evaluated the hardness of MnB_2 in different structures using the empirical model developed by Chen *et al.*,[44,45] which can be expressed as

$$H_V = 2(k^2G)^{0.585} - 3, \quad k = G/B, \tag{4}$$

where shear modulus G and bulk modulus B can be calculated by Voigt–Reuss–Hill approximation.[46] The calculated B, G, and H_V of different MnB_2 phases are listed in Table 3, together with the available theoretical data.[12,13,24,25] Our calculated B and G are in agreement with the other theoretical results. According to the empirical criterion proposed by Pugh,[47] if $B/G > 1.75$, the material behaves as ductility; otherwise, it exhibits brittle manner. In this work, the B/G ratio of $hP6$-MnB_2 and $oP12$-MnB_2 are 2.47 and 1.84, respectively, suggesting that they are ductile manner. While the B/G ratio of the other four phases of MnB_2 is less than 1.75, and therefore behaves brittle manner. In addition, our calculated H_V of $hP6$-MnB_2, $hR3$-MnB_2, $oP6$-MnB_2, $hP3$-MnB_2, $oI18$-MnB_2, and $oP12$-MnB_2 is 34.5 GPa, 35.8 GPa, 29.5 GPa, 9.48 GPa, 22.9 GPa, and 14.9 GPa, respectively. They are consistent with the other theoretical results[12,13,24,25] and the hardness sequence of MnB_2 should be $hR3 > hP6 > oP6 > oI18 > oP12 > hP3$. In general, the Vickers hardness H_V for a superhard material is higher than 40 GPa. Therefore, the $hP6$, $hR3$, and $oP6$ phases of MnB_2 are all potentially hard materials rather than superhard materials.

Table 3. Calculated bulk modulus B (in unit GPa), shear modulus G (in unit GPa), B/G, and Vickers's hardness H_V (in unit GPa) of different MnB_2 phases, together with theoretical results.

Phase	B_V	B_R	B	G_V	G_R	G	B/G	H_V	References
$hP6$	287.01	276.75	281.9	240.76	220.31	230.5	1.22	34.5	this work
			288.9			237.3	1.22	43.9	Cal.[24]
			281.4			232.7	1.21	35.8	Cal.[13]
$hR3$	284.80	275.35	280.0	246.51	222.53	234.5	1.19	35.82	this work
$oP6$	282.20	276.31	279.3	217.69	203.39	210.5	1.33	29.5	this work
$hP3$	291.85	275.28	283.6	118.36	111.58	114.9	2.47	9.48	this work
			288.0			135.0	2.13	16.5	Cal.[25]
$oI18$	313.58	303.39	308.5	200.97	190.18	195.6	1.58	22.96	this work
			308.0			195.0	1.58	22.5	Cal.[12]
$oP12$	270.06	229.19	249.6	142.78	128.88	135.82	1.84	14.90	this work

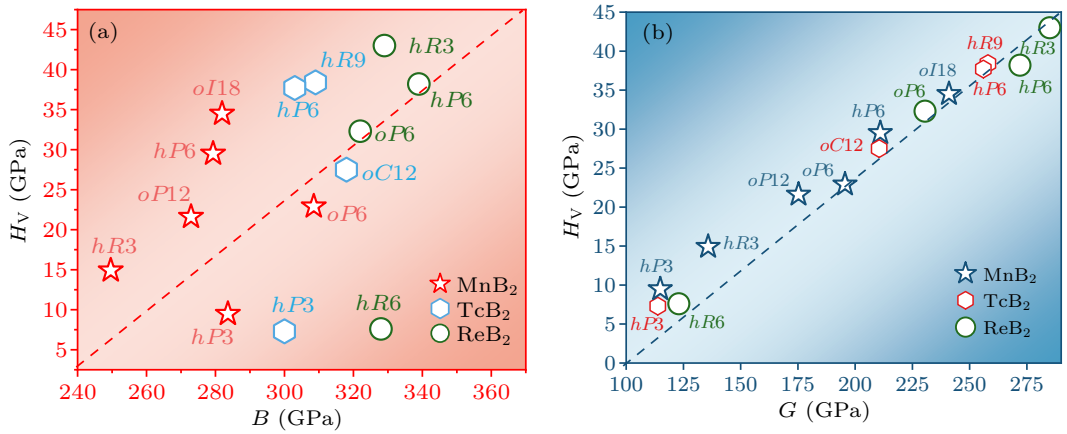


Fig. 3. Correlations between elastic modulus and hardness H_V of different MnB_2 phases: (a) bulk modulus B, and (b) shear modulus G. The data for TcB_2 and ReB_2 are taken from Refs. [29,30], respectively.

We have further analyzed the relationships between bulk modulus (and shear modulus) and hardness, as illustrated in Fig. 3. Generally, the bulk modulus of a material is considered to be a predictor of its hardness, and a higher bulk modulus value is associated with an increase in hardness.[48–50] However, as depicted in Fig. 3(a), there is no clear correlation between bulk modulus and hardness in both MnB_2, ReB_2 and TcB_2 diborides. That is to say, the relationship between

bulk modulus and hardness is not universally consistent, which is consistent with previous theoretical studies.[9,51,52] Meanwhile, it established a better linear correlation between hardness and shear modulus, as shown in Fig. 3(b). This is because of the shear modulus mainly describes the material's resistance to shear deformation, while hardness reflects the material's resistance to localized plastic deformation. This correlation is very interesting and suggests that the shear modulus can correctly provide an assessment of hardness for MnB_2 diborides. As shown in Table 3, the order of shear modulus for MnB_2 is $hR3 > hP6 > oI18 > oP6 > oP12 > hP3$, which is consistent with the order of hardness.

3.2.2. Anisotropic properties

It is important to fully describe the anisotropic behavior of different MnB_2 phases for understanding their mechanical properties. Different phases, due to their varying symmetries, affect the anisotropy of the material. Highly symmetric crystals, such as those with cubic symmetry, typically exhibit lower anisotropy, whereas crystals with lower symmetry, such as those with monoclinic or orthorhombic symmetry, show higher anisotropy. In general, the elastic anisotropy of a material can be described by the anisotropy index A^{U},[52] the compression anisotropy percentage A_{comp} and shear anisotropy percentage A_{shear}.[53] If these values of anisotropy are zero, which means the crystal is isotropic, otherwise, it is anisotropic. The larger the deviation, the stronger the elastic anisotropy. These anisotropy index can be calculated by the following formulas:

$$A^{\mathrm{U}} = \frac{5G_{\mathrm{V}}}{G_{\mathrm{R}}} + \frac{B_{\mathrm{V}}}{B_{\mathrm{R}}} - 6, \quad A_{\mathrm{comp}} = \frac{B_{\mathrm{V}} - B_{\mathrm{R}}}{B_{\mathrm{V}} + B_{\mathrm{R}}} \times 100\%,$$
$$A_{\mathrm{shear}} = \frac{G_{\mathrm{V}} - G_{\mathrm{R}}}{G_{\mathrm{V}} + G_{\mathrm{R}}} \times 100\%, \tag{5}$$

where B_{V} and G_{V} are bulk modulus and shear modulus of the Voigt scheme and B_{R} and G_{R} are bulk modulus and shear modulus of the Reuss scheme. The calculated A^{U}, A_{comp}, and A_{shear} of different MnB_2 structures are listed in Table 4. It can be seen that $oP12$-MnB_2 exhibits the largest A^{U} of 0.72, and $oI18$-MnB_2 possesses the lowest A^{U} of 0.32, which indicates that the anisotropy of $oP12$-MnB_2 is the greatest and that of $oI18$-MnB_2 is the smallest. So, the elastic anisotropy ranking of MnB_2 is $oP12 > hR3 > hP6 > oP6 > hP3 > oI18$, which is consistent with the results obtained by A_{shear}. Furthermore, the obtained maximum value ($\sim 8.19\%$) and minimum value ($\sim 1.05\%$) of A_{comp} belong to $oP12$-MnB_2 and $oP6$-MnB_2, respectively, indicating that $oP12$-MnB_2 exhibits the largest compression anisotropy, while $oP6$-MnB_2 possesses the smallest compression anisotropy. Thus, the order of compression anisotropy of MnB_2 should be $oP12 > hP3 > hP6 > hR3 > oI18 > oP6$.

Besides, the shear anisotropy factors A_1, A_2, and A_3 also serve as indices to quantify anisotropy among different crystal structures, which can be obtained by the following formulas:[54,55]

$$A_1 = \frac{4C_{44}}{C_{11} + C_{33} - 2C_{13}}, \quad A_2 = \frac{4C_{55}}{C_{22} + C_{33} - 2C_{23}},$$
$$A_3 = \frac{4C_{66}}{C_{11} + C_{22} - 2C_{12}}. \tag{6}$$

When A_1, A_2, and A_3 are equal to 1, the crystal structure is shearing isotropy. The calculated results of different MnB_2 structures are listed in Table 4. As shown, our obtained A_1 and A_2 of $oP12$-MnB_2 have the largest deviation from 1, suggesting that its shear anisotropy should be the highest at (100) and (010) planes. Meanwhile, $oP6$-MnB_2 should have the largest shear anisotropy in the (001) plane because its A_3 value deviates the most from 1. Further, it should be noted that the A_3 value of $hP6$-MnB_2 and the A_2 value of $hP3$-MnB_2 are both 1.00, which means that $hP6$-MnB_2 and $hP3$-MnB_2 should share isotropic in the (001) and (010) plane, respectively.

Table 4. Calculated elastic anisotropic indexes A^{U}, A_{comp}, A_{shear}, A_1, A_2, and A_3 for different MnB_2 phases.

Phase	A_1	A_2	A_3	A^{U}	A_{shear} (%)	A_{comp} (%)
$hP6$	0.95	0.95	1.00	0.50	4.44	1.82
$oP12$	1.67	0.65	0.75	0.72	5.12	8.19
$oP6$	0.95	0.67	1.29	0.37	3.40	1.05
$hP3$	1.14	1.00	1.14	0.36	2.94	2.92
$hR3$	1.03	0.93	0.93	0.57	5.11	1.69
$oI18$	1.15	1.08	0.94	0.32	2.76	1.65

To effectively describe the elastic anisotropy of different MnB_2 structures, we further plot the three-dimensional (3D) surface construction of bulk modulus B and Young's modulus E in this work. For different crystal systems, their direction-dependent quantities can be expressed as[56]

$$B = \left[(S_{11} + S_{12} + S_{13})l_1^2 + (S_{12} + S_{22} + S_{23})l_2^2 + (S_{13} + S_{23} + S_{33})l_3^2\right]^{-1}, \tag{7}$$
$$E = (l_1^4 S_{11} + 2l_1^2 l_2^2 S_{12} + 2l_1^2 l_3^2 S_{13} + l_2^4 S_{22} + 2l_2^2 l_3^2 S_{23} + l_3^4 S_{33} + l_2^2 l_3^2 S_{44} + l_1^2 l_3^2 S_{55} + l_1^2 l_2^2 S_{66})^{-1}, \tag{8}$$

where S_{ij} are the elements in the compliance tensor, and l_1, l_2, and l_3 are the direction cosines. The 3D surface constructions of bulk modulus B and Young's modulus E of different MnB_2 phases are shown in Figs. 4 and 5, respectively. It is evident from Fig. 4 that the bulk modulus in 3D graphs of different MnB_2 structures are not spherical, suggesting that their bulk modulus is indeed anisotropic. Generally, the greater the discrepancy between the 3D shape and the standard spherical shape, the more pronounced the anisotropy becomes. Accordingly, the anisotropic order of bulk modulus B of MnB_2 is $oP12 > hP3 > hP6 > hR3 > oI18 > oP6$, which is in agreement with the results of A_{comp}.

Similar to the bulk modulus B, the 3D graphs of Young's modulus E (see Fig. 5) also demonstrate non-spherical shapes, indicating that the Young's modulus of different MnB_2 structures is anisotropic. As depicted in Fig. 5, the anisotropy of $hR3$-MnB_2 is slightly lower than that of $oP12$-MnB_2, followed by $hP6$-MnB_2, $oP6$-MnB_2, and $hP3$-MnB_2, while $oI18$-MnB_2 exhibits the least anisotropy. Therefore, the anisotropic order of Young's modulus of MnB_2 is $oP12 > hR3 > hP6 > oP6 > hP3 > oI18$, which is consistent with the results of the anisotropic index A^{U}.

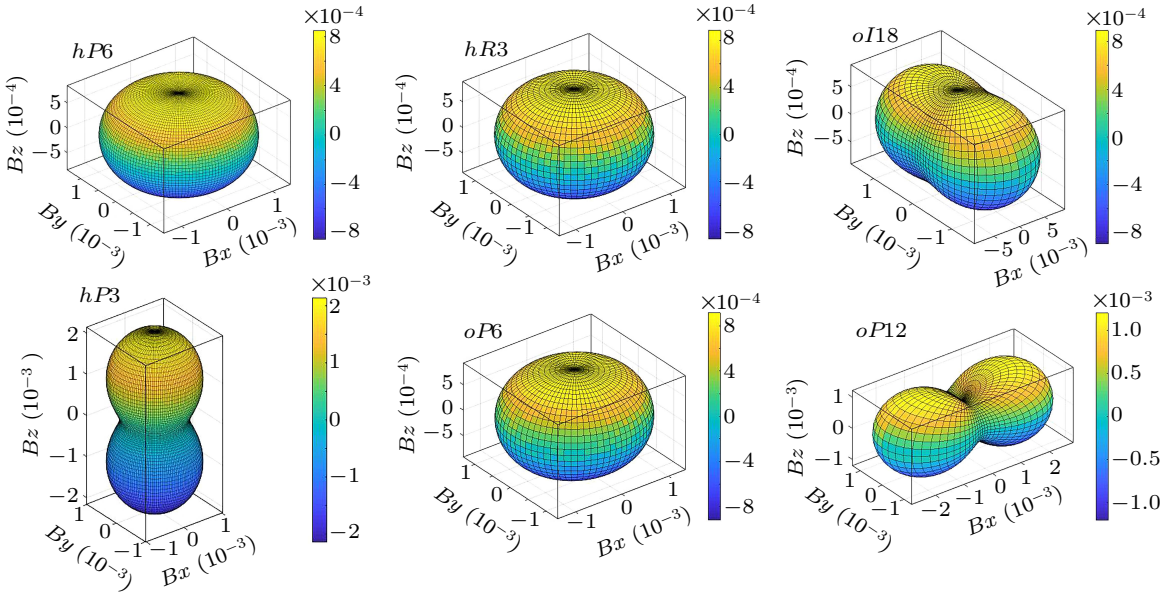


Fig. 4. The direction-dependent bulk modulus of different MnB_2 structures.

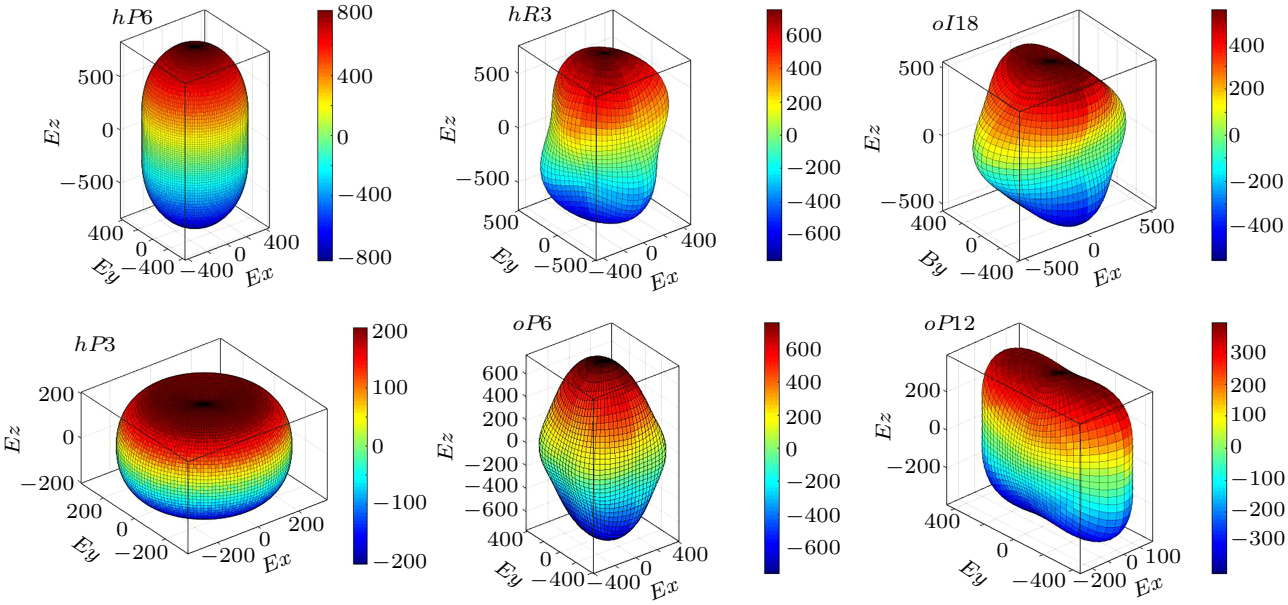


Fig. 5. The direction-dependent Young's modulus of different MnB_2 phases.

3.3. Debye temperature and minimum thermal conductivity

Debye temperature Θ is a crucial parameter closely associated with the elastic constants and the melting temperature of solids.[57] It reflects the vibrational frequency of atoms within the lattice and is influenced by both the crystal symmetry and the strength of the interatomic bonds. The different phases of MnB_2, owing to their unique atomic arrangements and interatomic interactions, which result in different Debye temperatures. In general, the Debye temperature Θ can be estimated using the following formula:

$$\Theta = \frac{h}{k_{\mathrm{B}}}\left[\frac{3n}{4\pi}\left(\frac{N_{\mathrm{A}}\rho}{M}\right)\right]^{1/3} v_{\mathrm{m}}, \tag{9}$$

where h is the Planck constant, k_{B} is the Boltzmann constant, n is the number of atoms per formula unit, N_{A} is Avogadro's number, M is the molecular mass in the formula unit, ρ is the

density, and v_m is the average sound velocity. Among them, v_m can be evaluated by

$$v_m = \left[\frac{1}{3}\left(\frac{2}{v_t^3}+\frac{1}{v_l^3}\right)\right]^{-1/3}, \tag{10}$$

where v_t is transverse sound velocity and v_l is longitudinal sound velocity, which can be calculated by Navier's equations:

$$v_l = \left(\frac{3B+4G}{3\rho}\right)^{1/2}, \quad v_t = \left(\frac{G}{\rho}\right)^{1/2}. \tag{11}$$

The calculated Debye temperature Θ and sound velocities v_t, v_l, v_m of different MnB_2 structures are listed in Table 5. It can be seen that *hR*3-MnB_2 has the largest Θ value of 664.06 K, while *hP*3-MnB_2 possesses the smallest Θ value of 468.58 K, which means that the *hR*3-MnB_2 should have stronger chemical bonds than the other MnB_2 phases, while *hP*3-MnB_2 should have the weakest chemical bonds. Moreover, the microhardness of the material is positively correlated with Debye temperature, so the microhardness order of MnB_2 should be $hR3 > hP6 > oP6 > oI18 > oP12 > hP3$.

Table 5. The density ρ (in units g/cm^3), transverse sound velocity v_t (in units km/s), longitudinal sound velocity v_l (in units km/s), average sound velocity v_m (in units km/s), Debye temperature Θ_D (in unit K), Poisson's ratio σ and Grüneisen parameter γ of different MnB_2 phases.

Phase	ρ	v_t	v_l	v_m	Θ	σ	γ	References
*hP*6	5.42	4.61	7.37	5.08	656.71	0.18	1.21	this work
*oP*6	5.40	4.42	7.21	4.88	629.48	0.20	1.28	this work
*hP*3	5.63	5.63	6.23	3.58	468.58	0.32	1.91	this work
						0.29		Cal.[25]
*hR*3	5.32	4.69	7.46	5.17	664.06	0.24	1.19	this work
*oI*18	5.67	4.15	7.09	4.60	604.30	0.23	1.45	this work
						0.24		Cal.[12]
*oP*12	5.77	3.43	6.11	3.82	504.15	0.54	1.60	this work

According to the obtained sound velocities v_t and v_l, we can further evaluate the Poisson's ratio σ and Grüneisen parameter γ as follows:

$$\sigma = \frac{1-2(v_t/v_l)^2}{2-2(v_t/v_l)^2}, \quad \gamma = \frac{3}{2}\left(\frac{1+\sigma}{2-3\sigma}\right). \tag{12}$$

The calculated σ and γ of different MnB_2 phases are also given in Table 5. In general, a small σ value indicates a more directional covalent bond, so the directionality degree of covalent bonds for MnB_2 should be $hP6 > oP6 > oI18 > hR3 > oP12 > hP3$. Additionally, Gruneisen parameter γ generally control a variety of important physical phenomena, including thermal expansion, conduction, acoustic wave absorption, and the temperature dependence of elastic properties. A high γ value typically suggests a strong crystal anharmonicity.[58] Therefore, the anharmonic order of MnB_2 can be arranged as $hP3 > oP12 > oI18 > oP6 > hP6 > hR3$.

Studying the minimum thermal conductivity will help to understand the performance of different MnB_2 phases at high temperatures and expand their applications across various fields.[5,59] Therefore, we employed two theoretical models[60,61] to evaluate the minimum thermal conductivity of different MnB_2 phases. Among them, the Clarke's model can be expressed as

$$k_{min} = 0.87 k_B M_a^{-2/3} E^{1/2} \rho^{1/6}, \tag{13}$$

$$M_a = \frac{M}{mN_A}, \tag{14}$$

where k_B is Boltzmann's constant, M_a denotes average mass per atom, E is Young's modulus, ρ is density, M delegates molar mass, m is total number of atoms in the unit cell, and N_A is Avogadro's number. Moreover, the Cahill's model can be determined as

$$k_{min} = \frac{k_B}{2.48} n^{2/3} (v_l + 2v_t), \tag{15}$$

where n is the density of atomic numbers per unit volume. The obtained minimum thermal conductivity of different MnB_2 phases is listed in Table 6. As shown, the k_{min} values obtained from the Cahill's model are consistently greater than those from the Clarke's model, because the Clark's model does not take into account the contribution of the optical phonon modes to the thermal conductivity in this work. Moreover, we can find that the *hR*3-MnB_2 possesses the largest k_{min} value in both Clarke's and Cahill's models, followed by *hP*6-MnB_2, *oP*6-MnB_2, *oI*18-MnB_2, and *oP*12-MnB_2, while *hP*3-MnB_2 has the smallest k_{min} value. In general, materials with a minimum thermal conductivity of less than 1.25 W·m^{-1}·K^{-1} are suitable for thermal barrier coating applications.[62] It is worth noting that the minimum thermal conductivity of different MnB_2 phases studied in this work is between 1.62 W·m^{-1}·K^{-1} and 2.16 W·m^{-1}·K^{-1}, indicating that they are all not suitable as thermal barrier coating materials.

Table 6. Calculated minimum thermal conductivity k_{min} (in units W·m^{-1}·K^{-1}) of different MnB_2 phases.

Phase	Clarke model		Cahill model	
	M_a (10^{-26})	k_{min}	n (10^{29})	k_{min}
*hP*6	4.24	2.16	1.280	2.35
*oP*6	4.24	2.08	1.272	2.26
*hR*3	4.24	2.17	1.272	2.37
*hP*3	4.24	1.62	1.361	1.83
*oI*18	4.24	2.05	1.337	2.24
*oP*12	4.24	1.74	1.361	1.91

4. Conclusion

In summary, we utilized the structure prediction algorithm CALYPSO combined with first-principles calculations to investigate the structures stability, elastic anisotropy, and thermal conductivity of MnB_2 in different crystal structures. Our findings revealed that *hP*6-MnB_2, *hP*3-MnB_2, *oP*6-MnB_2, *hR*3-MnB_2, *oP*12-MnB_2, and *oI*18-MnB_2 exhibit both

mechanical and dynamical stabilities under ambient conditions. Based on the formation enthalpies, the phase stability order of MnB_2 is determined as $hP6 > hR3 > oP6 > oI18 > oP12 > hP3$. Besides, Vickers hardness calculations suggested that $hP6$, $hR3$, $oP6$, and $oI18$ of MnB_2 have potential as hard materials, whereas $hP3$ and $oP12$ are not suitable as hard materials. Additionally, the anisotropic order of bulk modulus B of MnB_2 should be $oP12 > hP3 > hP6 > hR3 > oI18 > oP6$, while the anisotropic order of Young's modulus is $oP12 > hR3 > hP6 > oP6 > hP3 > oI18$. Meanwhile, the study of Debye temperature shows that the microhardness order of MnB_2 should be $hR3 > hP6 > oP6 > oI18 > oP12 > hP3$. Finally, the minimum thermal conductivity of MnB_2 in different structures is further estimated, and the order is $hR3 > hP6 > oP6 > oI18 > oP12 > hP3$. Since the calculated minimum thermal conductivity of different MnB_2 phases is all higher than 1.25 $W{\cdot}m^{-1}{\cdot}K^{-1}$, indicating that they are not suitable as thermal barrier coating materials.

Acknowledgements

Project supported by the Natural Science Basic Research Program of Shaanxi Province, China (Grant No. 2024JC-YBQN-0044), the National Natural Science Foundation of China (Grant No. 11904282), and the Doctoral Scientific Research Foundation of Xi'an University of Science and Technology (Grant No. 2018QDJ029).

References

[1] Wang Y X, Yan Z X and Liu W 2020 *RSC. Adv.* **10** 37142
[2] Lazar P, Chen X Q and Podloucky R 2009 *Phys. Rev. B* **80** 012103
[3] Liang Y and Zhang B 2007 *Phys. Rev. B* **76** 132101
[4] Vogt T, Schneider G, Hriljac J A, Yang G and Abell J S 2001 *Phys. Rev. B* **63** 220505
[5] Wang Z, Kuang X, Yu G, Zhao P, Zhong H and Yuan S 2021 *Phys. Rev. B* **104** 155110
[6] Zhong M M, Huang C and Tian C L 2017 *Int. J. Mod. Phys. B* **31** 1750131
[7] Steinki N, Winter J L and Schulze Grachtrup D 2017 *J. Alloys Compd.* **695** 2149
[8] Pei C Y and Zhang J F 2022 *Sci. China Phys. Mech. Astron.* **65** 287412
[9] Li P, Ma L, Peng M, Shu B and Duan Y 2018 *J. Alloys Compd.* **747** 905
[10] Liang Y, Wu Z and Wang S 2015 *AIP Adv.* **5** 117208
[11] Gou H, Steinle-Neumann G, Bykova E, Nakajima Y, Miyajima N, Li Y, Ovsyannikov S V, Dubrovinsky L S and Dubrovinskaia N 2013 *Appl. Phys. Lett.* **102** 061906
[12] Xu C, Bao K, Ma S, Cui T, Ma Y, Wei S, Shao Z, Xiao X, Feng X and Cui T 2017 *RSC Adv.* **7** 10559
[13] Niu H, Chen X Q, Ren W, Zhu Q, Oganov A R, Li D and Li Y 2014 *Phys. Chem. Chem. Phys.* **16** 15866
[14] Liang Y, Wu Z, Yuan X, Zhang W and Zhang P 2016 *Nanoscale* **8** 1055
[15] Mohn P and Pettifor D G 1988 *J. Phys. C: Solid State Phys.* **21** 2829
[16] Ma S, Bao K, Tao Q, Zhu P, Ma T, Liu B, Liu Y and Cui T 2017 *Sci. Rep.* **7** 43759
[17] Ishii T, Shimada M and Koizumi M 1983 *J. Appl. Phys.* **54** 6907
[18] Qu Z Y, Han F J and Yu T 2020 *Phys. Rev. B* **102** 075431
[19] Gou H, Tsirlin A A, Bykova E, Abakumov A M, Van Tendeloo G, Richter A, Ovsyannikov S V, Kurnosov A V, Trots D M, Konôpková Z, Liermann H P, Dubrovinsky L and Dubrovinskaia N 2014 *Phys. Rev. B* **89** 064108
[20] Sun Y, Duan Y, Li X, Xu X, Yao X, Liu S, Yin H, Wang B, Liu Y and Zhang X 2023 *Int. J. Quantum Chem.* **123** e27117
[21] Liang Y, Xu M and Qu Z 2021 *J. Mater. Chem. C* **9** 8258
[22] Cely A, Ter Genius L E and Lundstrom T 1978 *J. Less. Common. Met.* **61** 193
[23] Asokamani R S, Vajeeston P R and Ravindra P 1970 *Acta. Chem. Scand.* **24** 1791
[24] Aydin S and Simsek M 2009 *Phys. Rev. B* **80** 134107
[25] Wang B, Li X, Wang Y X and Tu Y F 2011 *J. Phys. Chem. C* **115** 21429
[26] Fan J, Bao K, Jin X, Meng X, Duan D, Liu B and Cui T 2012 *J. Mater. Chem.* **22** 17630
[27] Gao B, Gao P, Lu S, Lv J, Wang Y and Ma Y 2019 *Sci. Bull.* **64** 301
[28] Wang Y, Lv J, Zhu L and Ma Y 2012 *Comput. Phys. Commun.* **183** 2063
[29] Wang Y X, Wu H, Xie W N and Wang X F 2024 *J. Appl. Phys.* **135** 205901
[30] Wang Y X, Yan Z X, Liu W and Zhou G L 2019 *J. Appl. Phys.* **126** 135901
[31] Wang X F, Wang Y X, Wu H and Xie W N 2024 *Appl. Phys. A* **130** 414
[32] Monkhorst H J and Pack J D 1976 *Phys. Rev. B* **13** 5188
[33] Payne M C, Teter M P and Allan D C 1992 *Rev. Mod. Phys.* **64** 1045
[34] Milman V and Winkler B 2000 *Int. J. Quantum Chem.* **77** 895
[35] Parlinski K, Li Z Q and Kawazoe Y 1997 *Phys. Rev. Lett.* **78** 4063
[36] Alfè D 2009 *Computer Phys. Commun.* **180** 2622
[37] Xie W N, Wang Y X, Y Z X and Liu W 2023 *Eur. Phys. J. B* **96** 64
[38] Wang Y X, Yan Z X and Liu W 2019 *Philos. Mag.* **99** 2321
[39] epkowski S P 2020 *Phys. Rev. B* **102** 134116
[40] Luo F, Fu M, Ji G F and Chen X R 2010 *Chin. Phys. B* **19** 027101
[41] Wu Z, Zhao E, Xiang H, Hao X, Liu X and Meng J 2007 *Phys. Rev. B* **76** 054115
[42] Perdew J P, Burke K and Ernzerhof M 1996 *Phys. Rev. Lett.* **77** 3865
[43] Beckstein O, Klepeis J E, Hart G LW and Pankratov O 2001 *Phys. Rev. B* **63** 134112
[44] Chen X Q, Niu H, Li D and Li Y 2011 *Intermetallics* **19** 1275
[45] Lech A T, Turner C L, Mohammadi R, Tolbert S H and Kaner R B 2015 *Proc. Natl. Acad. Sci. USA* **112** 3223
[46] Hill R 1952 *Proc. Phys. Soc. A* **65** 349
[47] Pugh S F 1954 *XCII. 1954 Phil. Mag.* **45** 823
[48] Ivanovskii A L 2012 *Prog. Mater. Sci.* **57** 184
[49] Gilman J J 2009 *Chemical Hardness* (John Wiley & Sons, Inc.) pp. 189–196
[50] Teter Daid M 1998 *MRS Bull.* **23** 22
[51] Levine J B, Tolbert S H and Kaner R B 2009 *Adv. Funct. Mater.* **19** 3519
[52] Ranganathan S I and Ostoja-Starzewski M 2008 *Phys. Rev. Lett.* **101** 055504
[53] Vahldiek F W and Mersol S A 1968 held on June 13–15, 1967, in Dayton Ohio. Sponsored by the Ceramics and Branch of the air Force Materials Laboratory, United States Air Force (Boston, MA: Springer US)
[54] Ravindran P, Fast L, Korzhavyi P A, Johansson B, Wills J and Eriksson O 1998 *J. Appl. Phys.* **84** 4891
[55] Ma Y, Zhang X, Ma H, Guo H and Wang F 2022 *Solid State Commun.* **353** 114869
[56] Qu D, Li C, Bao L, Kong Z and Duan Y 2020 *J. Phys. Chem. Solids* **138** 109253
[57] Anderson O L 1963 *J. Phys. Chem. Solids* **24** 909
[58] Jin Y Y, Zhang J Q, Ling S, Wang Y Q, Li S, Kuang F G, Wu Z Y and Zhang C Z 2022 *Chin. Phys. B* **31** 116104
[59] Cheng Y, Fan Z, Zhang T, Nomura M, Volz S, Zhu G, Li B and Xiong S 2023 *Mater. Today Phys.* **35** 101093
[60] Clarke D R 2003 *Surf. Coat. Tech.* **163** 67
[61] David G, Cahill and S 1992 *Phys. Rev. B* **46** 6131
[62] Liu Y, Cooper V R, Wang B, Xiang H, Li Q, Gao Y, Yang J, Zhou Y and Liu B 2019 *Mater. Res. Lett.* **7** 145